

Short Communication: Subcellular Motion Compensation for Minimally Invasive Microscopy, In Vivo: Evidence for Oxygen Gradients in Resting Muscle

James L. Schroeder, Merav Luger-Hamer, Randall Pursley, Tom Pohida, Chris Chefd'Hotel, Peter Kellman and Robert S. Balaban

Circ. Res. 2010;106;1129-1133; originally published online Feb 18, 2010;

DOI: 10.1161/CIRCRESAHA.109.211946

Circulation Research is published by the American Heart Association, 7272 Greenville Avenue, Dallas, TX 75214

Copyright © 2010 American Heart Association. All rights reserved. Print ISSN: 0009-7330. Online ISSN: 1524-4571

The online version of this article, along with updated information and services, is located on the World Wide Web at:

<http://circres.ahajournals.org/cgi/content/full/106/6/1129>

Data Supplement (unedited) at:

<http://circres.ahajournals.org/cgi/content/full/CIRCRESAHA.109.211946/DC1>

Subscriptions: Information about subscribing to Circulation Research is online at
<http://circres.ahajournals.org/subscriptions/>

Permissions: Permissions & Rights Desk, Lippincott Williams & Wilkins, a division of Wolters Kluwer Health, 351 West Camden Street, Baltimore, MD 21202-2436. Phone: 410-528-4050. Fax: 410-528-8550. E-mail:
journalpermissions@lww.com

Reprints: Information about reprints can be found online at
<http://www.lww.com/reprints>

Short Communication

Subcellular Motion Compensation for Minimally Invasive Microscopy, In Vivo

Evidence for Oxygen Gradients in Resting Muscle

James L. Schroeder, Merav Luger-Hamer, Randall Pursley, Tom Pohida, Chris Chefd'Hotel, Peter Kellman, Robert S. Balaban

Rationale: In vivo microscopy seeks to observe dynamic subcellular processes in a physiologically relevant context. A primary limitation of optical microscopy in vivo is tissue motion, which prevents physiological time course observations or image averaging.

Objective: To develop and demonstrate motion compensation methods that can automatically track image planes within biological tissues, including the tissue displacements associated with large changes in blood flow, and to evaluate the effect of global hypoxia on the regional kinetics and steady state levels of mitochondrial NAD(P)H.

Methods and Results: A dynamic optical microscope, with real-time prospective tracking and retrospective image processing, was used collect high-resolution images through cellular responses to various perturbations. The subcellular metabolic response to hypoxia was examined in vivo. Mitochondria closest to the capillaries were significantly more oxidized at rest ($67 \pm 3\%$) than the intrafibrillar mitochondria ($83 \pm 3\%$; $P < 0.0001$) in the same cell.

Conclusions: These data are consistent with the hypothesis that a significant oxygen gradient from capillary to muscle core exists at rest, thereby reducing the oxidative load on the muscle cell. (*Circ Res.* 2010;106:1129-1133.)

Key Words: two-photon excitation microscopy ■ perivascular mitochondria ■ NADH fluorescence
■ mouse skeletal muscle ■ redox state

Recently developed fluorescent probes for gene expression, cellular milieu, and enzyme activities can be coupled with multi-photon microscopy,¹ with its improved penetration, sensitivity, and information content,² to provide a unique window into cell physiology. Most in vivo microscopy preparations are mechanically isolated thin (<1 mm) tissues or tissues constrained using a cover glass. Without such constraints, physiological and perturbation-related motion prevents temporal signal averaging and complicates serial measurements of a given region.^{1,3} While imaging restrained, translucent specimens has yielded many insights, the ability to observe thick tissues would allow observation of processes in a broader range of experimental models and may simplify preparations.

In several tissues, including skeletal muscle, liver, kidney, and brain, we find drift movement significantly exacerbated by physiological perturbation ($\pm 100 \mu\text{m}/\text{min}$). These displacements may be caused by changes in blood volume, flow, or cellular metabolism, resulting in a gradual redistribution of fluid between plasma, extracellular space, and intracellular space. Movement is amplified in larger tissues, where small percent changes lead to larger microscopic displacements.

We have addressed translational movement prospectively, using a dynamic microscope, and corrected for residual nontranslational movement retrospectively. Our objective was to follow tissue motions on the order of $100 \mu\text{m}$, while retaining an in-plane resolution of $< 2 \mu\text{m}$. This was accomplished by real-time tracking of 3D tissue using a dynamic stage, focusing unit, and computer system, adaptable to most microscopes. The utility of this approach was demonstrated by acquiring high-resolution images of the mouse skeletal muscle, vasculature, and mitochondrial distribution, in vivo, to monitor the redox state of the different intracellular pools of mitochondria under resting and hypoxic conditions.

The determination of vascular structure and flow relative to cellular morphology and metabolism may be critical to the understanding of microvascular flow regulation. Mitochondrial NAD(P)H fluorescence is an intrinsic probe for monitoring the redox effects of hypoxia or ischemia in vivo^{4,5} as well as in vitro.⁶ The [NAD(P)H]/[NAD(P)] ratio reflects the redox state of the mitochondria, and requires the determina-

Original received October 24, 2009; revision received February 8, 2010; accepted February 10, 2010.

From the Laboratory of Cardiac Energetics (J.L.S., M.L.-H., P.K., R.S.B.), National Heart, Lung, and Blood Institute, NIH, Bethesda, Md; Signal Processing and Instrumentation Section (R.P., T.P.), Center for Information Technology, NIH, Bethesda, Md; and Department of Imaging and Visualization (C.C.), Siemens Research, Princeton, NJ.

Correspondence to Robert Balaban, 10 Center Dr, 10-CRC-4-1581, Bethesda, MD 20892. E-mail balabanr@nhlbi.nih.gov

© 2010 American Heart Association, Inc.

Circulation Research is available at <http://circres.ahajournals.org>

DOI: 10.1161/CIRCRESAHA.109.211946

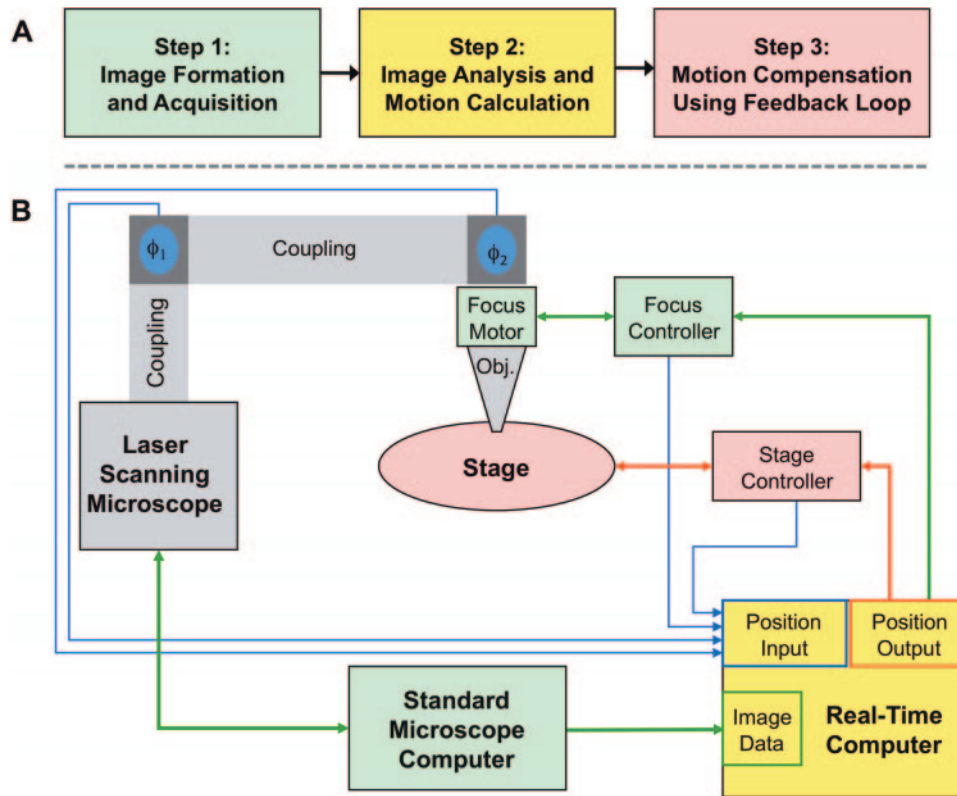


Figure 1. Real-time microscope setup. **A**, Flow chart depicting 3 stages of motion compensation, color-coded to microscope components. **B**, Schematic of microscope setup, with **arrows** indicating data connections. The diagram depicts inverted microscope with periscope; setup is also adaptable to upright microscope.

tion of the fluorescence associated with both the fully reduced and fully oxidized NAD(P)H pool. Limited information is available on the subcellular metabolic responses of different cellular pools of mitochondria under any perturbation, *in vivo*, and such information could provide evidence for topological differences in cellular metabolism. We selected the use of hypoxia as an experimental perturbation because it is physiologically significant, results in substantial motion, and provides a fully reduced state for determining $[NAD(P)H]/[NAD(P)]$ ratio in muscle.

Several technical and physiological questions were addressed in this study. (1) Can the tracking scheme compensate for the large volume shifts occurring during hypoxia to monitor the vascular structure and mitochondria redox response? (2) Do all of the fiber types in a given field of view follow the same time course of increased mitochondrial $[NAD(P)H]$ in hypoxia? (3) Are the cellular pools of mitochondria at the same NAD(P)H redox state in resting muscle, reflecting regional differences in metabolism or oxygen delivery?

Methods

A commercial multiphoton excitation microscopy setup for *in vivo* imaging⁷ was coupled to a real-time computer (Figure 1). Prospective motion tracking was accomplished by sequentially acquiring orthogonal image planes, calculating tissue displacements from the images and offsetting motion to maintain a fixed relationship between the objective and the area of interest.

Image acquisition sequentially alternated between the 2 orthogonal imaging planes. An *x-y* image was acquired using the microscope galvo-mirrors. An *x-z* image was acquired by holding the *y* galvo-

mirror stationary while line scanning in *x* and ramping the focusing motor in *z*. Both the *x-y* and *x-z* image planes were recorded by the real-time computer in parallel to the normal acquisition of the microscope system.

Image analysis compared each incoming image with a previously acquired image. At the start of motion tracking, one image from each acquisition plane was stored as a reference. Each subsequent image was compared to the reference image using normalized 2D cross-correlation to determine displacement (Figure 2). The stage was automatically adjusted based on the calculated offset to compensate for the motion.

The imaging setup simultaneously acquired 2 channels (expanded Methods section, available in the Online Data Supplement at <http://circres.ahajournals.org>). An emission centered on 460 nm originated from NAD(P)H.⁴ An emission centered on 590 nm detected di-8-ANEPPS dye (di-8-[butyl] amino-naphthyl-ethylene-pyridinium-propyl-sulfonate) in vascular endothelial cells, and this channel was used for tracking. Dye in the vasculature provided visualization of flow by negative contrast of moving red blood cells.

To correct for small in-plane deformations, a retrospective non-rigid body compensation was applied using deformable registration.⁸ A motion map was calculated for each frame by iteratively maximizing the local cross-correlation image subsets at different resolutions. The motion map calculation used the spatial information in the vascular/dye channel and then applied to both channels. To optimally filter the registered time course images, a principal component analysis was conducted (Online Data Supplement).

Free-breathing mice were anesthetized via a mask and the lower leg was immobilized by clamping just above the foot without obstructing proximal blood flow. The skin and surface fascia over the muscle were removed. A clear optical gel⁷ coupled the objective to the tissue. Alternatively, buffered saline, flowing from the objective to the muscle was used to deliver compounds (Online Data Supplement). A field-of-view showing vasculature and blood flow was selected $\approx 100 \mu\text{m}$ below the surface.

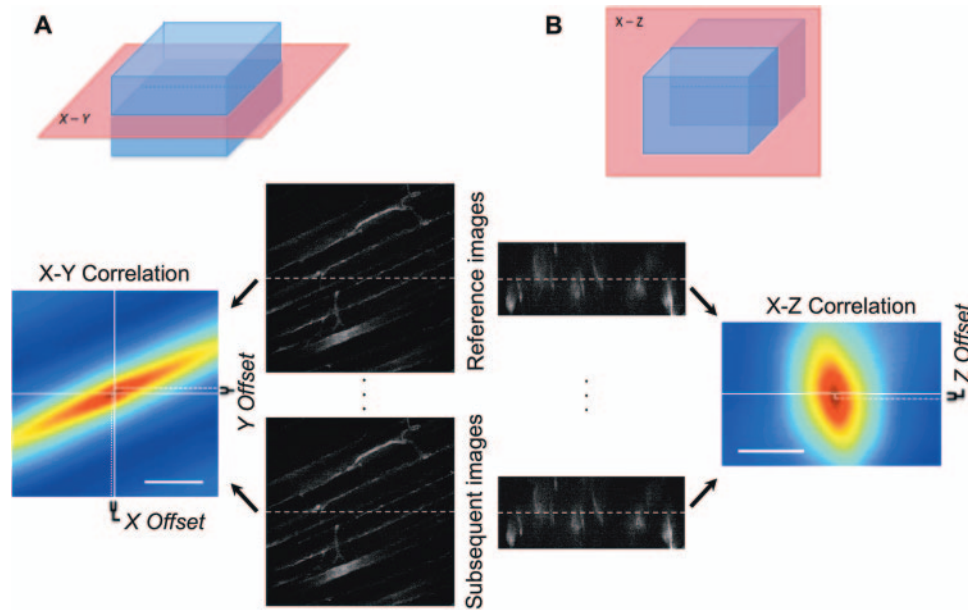


Figure 2. Acquisition and analysis of image data. Scanning alternates between acquiring an x-y image (A) and an x-z image (B). At the start of tracking, 1 x-y image and 1 x-z image are saved as a reference images. Subsequent images are compared to the reference using normalized cross-correlation. The correlation image maximum is offset from image origin in proportion to the motion displacement.

Protocols to validate resolution during motion tracking and to determine fully oxidized NAD(P)H fluorescence signal after uncoupler was performed (Online Data Supplement). In the hypoxia protocol, 6 animals underwent a systemic hypoxia, through death, to generate the fully reduced NAD(P)H signal. After collecting a control period breathing room air, the ventilated gas was switched to nitrogen to induce global hypoxia. Blood oxygenation of the animal was monitored with a pulse oximeter in 50% of the studies to confirm systemic hypoxia. The time course response was monitored in both image channels, until the vascular images showed a cessation or reversal of red cell flow and mitochondrial NAD(P)H fluorescence reached a plateau, several minutes after death.

Results

Motion compensation during the hypoxia experiments averaged $28 \pm 5 \mu\text{m}$ per minute for up to 10 minutes ($n=6$, SE). Tracking was successful in maintaining the plane of interest within $<2 \mu\text{m}$. Image data were significantly improved using the deformable registration algorithm (Online Video 1). During hypoxia, the NAD(P)H signal increased (50% half-maximal [NAD(P)H] in 35 ± 5 seconds, $n=6$, SE), visible in the filtered data and the calculated NAD(P)H/NAD(P) ratio images (Online Video 2). Two principle components of the hypoxia time courses reached significance in the experiments (expanded Results section in the Online Data Supplement). The primary and secondary components were linear combinations of each other ($R^2=0.73 \pm 0.07$, $n=6$, SE), so within the temporal and spatial resolution of our experiments, no multimodal distribution of kinetics between cells or mitochondrial pools occurred within muscle. Thus, the kinetic response of NAD(P)H fluorescence to hypoxia was statistically identical in all fiber types and intracellular pools.

The percentage change in NAD(P)H fluorescence was significantly higher in the perivascular regions than the core

or intrafibrillar regions. This indicates that the outer regions of cells were significantly more oxidized than the core under control conditions (Figure 3). NAD(P)H/NAD(P) images were calculated using regional fluorescence as [resting level]/[hypoxic level]. Mid-cell cross-sections were identified by fiber dimension and the absence of capillaries on the surface. Mid-cell NAD(P)H/NAD(P) profiles were generated for all datasets (expanded Results section in the Online Data Supplement). The NAD(P)H ratio at rest averaged $67 \pm 3\%$ reduced in perivascular regions and $83 \pm 3\%$ reduced in intrafibrillar regions ($n=8$ cells from 6 animals; $P<0.0001$, paired t test; SE).

Discussion

The motion compensation methods described are capable of tracking regions within a cell, in vivo, during physiological perturbations. Using prospective tracking and retrospective image correction, we demonstrated improved average image signal-to-noise ratios with minimal degradation of spatial resolution. This approach is useful in producing in vivo images with high signal-to-noise ratios and enables in vivo fluorescence methods with low signal-to-noise, such as spectral imaging, that require extensive signal averaging. It also allows continuous measurement of a set of cells through time during a physiological perturbation, in vivo.

Given the extensive motion associated with hypoxia, it would have been extremely difficult to observe intracellular events through this perturbation without the tracking system. The topology of the fluorescence was consistent with mitochondrial NAD(P)H, and fluorescence intensity responded appropriately to uncoupler and hypoxia. The mean increase in NAD(P)H fluorescence during hypoxia over the entire field-of-view was approximately 50%, consistent with whole muscle measurements made with single photon excitation

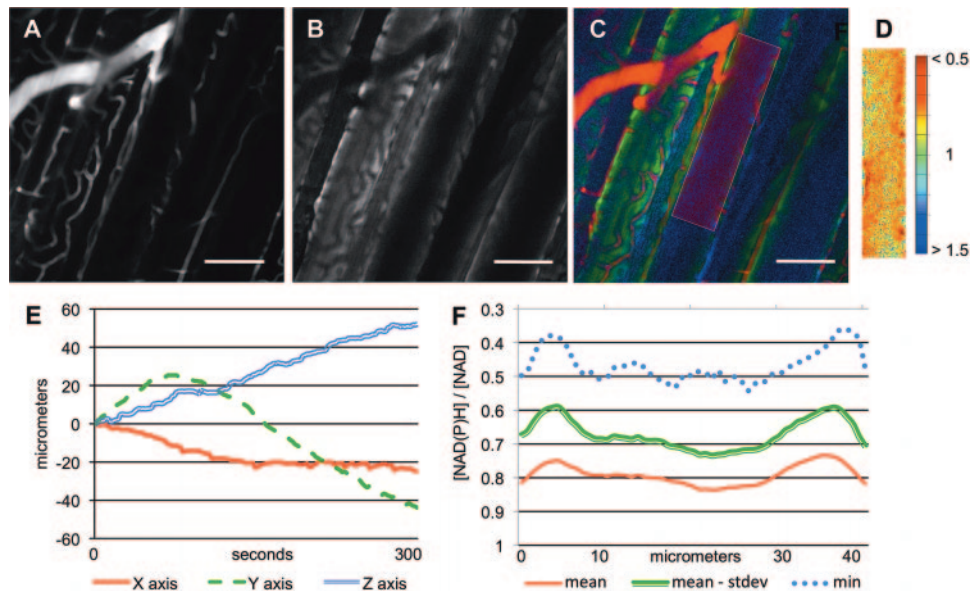


Figure 3. NAD(P)H topology during hypoxia. Mean image of vasculature channel (A), mean NAD(P)H channel (B), and mean combined channels (C) with vasculature (red), NAD(P)H (green), and [NAD(P)H]/[NAD] ratio at rest (blue). Scale bars: 50 μm . D, Magnification of a cell meeting central cross-section criteria, showing resting [NAD(P)H]/[NAD] ratio with color lookup table indicated. E, Amount of x-, y-, and z-stage movement required to compensate for motion during acquisition. F, Horizontal mean profile of [NAD(P)H]/[NAD] ratio across the magnified cell, illustrating the greater mean reduction and pockets of greatest reduction clustered toward the cell periphery.

averaged over large regions of muscle^{3,7,9} or in arteriole versus venule regions of capillaries. However, these whole muscle studies average NAD(P)H redox state over multiple cells, whereas we demonstrate that the redox state is dependent on position within a cell.

These results indicate that either the metabolic state in mitochondria in the perivascular region is substantially different than in the intrafibrillar pool, or that a significant oxygen gradient exists from the outer regions of the cell, close to the capillary networks, to the center of the cell. It has been suggested that the perivascular mitochondria function, composition, and susceptibility to flow insults¹⁰ may be different from the intrafibrillar mitochondria.^{10,11} However, none of these observations would predict a resting difference in NAD(P)H redox state.

A likely reason for the NAD(P)H redox gradient would be an oxygen gradient from the capillaries to the center of the cell. The existence of an oxygen gradient across single cells or within the muscle⁵ has been a controversial subject for many years.¹² However, the larger concentration of mitochondria at the vascular interface¹³ could support steep oxygen gradients because the cellular oxygen consumption capacity is focused in this region.¹⁴ Supporting this hypothesis is the calculation that the oxygen consumption capacity of the perivascular regions is ≈ 4 -fold greater than the core of the muscle cell.¹¹ This electron microscopy estimate of the relative distribution of mitochondria could be an underestimate; 3D views of the tissue structure show a large fraction of the mitochondria situated near the capillaries (Online Videos 3 and 4).

The distribution of mitochondria at the periphery of the cell requires energy transfer within the cell to be dependent on the diffusion of ATP, creatine phosphate, and creatine and not the faster diffusion of oxygen. This dependence on metabolite diffusion and associated high concentration of

metabolites may contribute to the metabolic homeostasis across the muscle fiber.¹⁴ We speculate that the high concentration of mitochondria located at the capillaries results in the generation of significant oxygen gradients across cells in low-flow resting conditions. This oxygen gradient may be beneficial in reducing the concentration of oxygen in the cell volume and preventing oxidative damage, relying on the high concentration of metabolites to maintain the distribution of potential energy throughout the cell. The distribution of mitochondria may reflect a strategy to minimize cellular oxygen tension, reducing the potential toxic effects of oxygen in the cytosol.

Sources of Funding

Supported by the NIH/National Heart, Lung, and Blood Institute Division of Intramural Research (grant HL004610-02).

Disclosures

None.

References

1. Rubart M. Two-photon microscopy of cells and tissue. *Circ Res*. 2004; 95:1154–1166.
2. Denk W, Strickler JH, Webb WW. Two-photon laser scanning fluorescence microscopy. *Science*. 1990;248:73–76.
3. Rothstein EC, Carroll S, Combs CA, Jobsis PD, Balaban RS. Skeletal muscle NAD(P)H two-photon fluorescence microscopy in vivo: topology and optical inner filters. *Biophys J*. 2005;88:2165–2176.
4. Chance B, Cohen P, Jobsis F, Schoener B. Intracellular oxidation-reduction states in vivo. *Science*. 1962;137:499–508.
5. Toth A, Pal M, Tischler ME, Johnson PC. Are there oxygen-deficient regions in resting skeletal muscle? *Am J Physiol*. 1996;270: H1933–H1939.
6. Eng J, Lynch RM, Balaban RS. NADH fluorescence spectroscopy and imaging of isolated cardiac myocytes. *Biophys J*. 1989;55:621–630.
7. Rothstein EC, Nauman M, Chesnick S, Balaban RS. Multi-photon excitation microscopy in intact animals. *J Microsc*. 2006;222:58–64.

8. Hermosillo G, ChefHotel C, Faugeras O. Variational methods for multimodal image matching. *Int J Comp Vis.* 2002;50:329–343.
9. Mayevsky A, Rogatsky GG. Mitochondrial function in vivo evaluated by NADH fluorescence: from animal models to human studies. *Am J Physiol Cell Physiol.* 2007;292:C615–C640.
10. Benson DW, Weinstein ES, Niffenegger J, Yokum M, Fry DE. Subpopulations of skeletal muscle mitochondria: response to ischemia. *Am Surg.* 1985;51:682–686.
11. Philippi M, Sillau AH. Oxidative capacity distribution in skeletal muscle fibers of the rat. *J Exp Biol.* 1994;189:1–11.
12. Jones DP. Intracellular diffusion gradients of o_2 and ATP. *Am J Physiol.* 1986;250:C663–C675.
13. Henneman E, Olson CB. Relations between structure and function in the design of skeletal muscles. *J Neurophysiol.* 1965;28:581–598.
14. Mainwood GW, Rakusan K. A model for intracellular energy transport. *Can J Physiol Pharmacol.* 1982;60:98–102.

Novelty and Significance

What Is Known?

- Visualization of metabolic and signaling events within cells in vivo is required to fully understand many clinically relevant physiological processes.
- Tissue motion is a major limitation for micrometer-resolution imaging in vivo.
- The existence of subcellular oxygen tension gradients in vivo has been speculated to be important in metabolic signaling and protection from free radical damage.

What New Information Does This Article Contribute?

- A strategy is presented to compensate for tissue motion while maintaining micrometer resolution using an image-guided dynamic microscope.
- Muscle mitochondria, which use oxygen, are concentrated near vascular capillaries, which supply oxygen.
- Mitochondria in close proximity to vessels were shown to be more oxidized than mitochondria in the center of the cell, consistent with the existence of a gradient in oxygen tension across the cell, at rest.

In vivo observations of intracellular signaling and metabolic responses during cellular processes are complicated by the lack of robust methods to compensate for tissue motion associated with physiological perturbations in bulk tissue. We report a strategy to compensate for tissue motion using an image-guided dynamic microscope and retrospective image analysis. These imaging methods expand possible targets for in vivo intracellular observations to new tissue preparations and physiological experiments, while improving image quality. Using these methods, in vivo measurements of the subcellular metabolic response to hypoxia were made in mouse skeletal muscle for the first time. Micrometer-resolution images of mitochondrial NAD(P)H autofluorescence showed that a large fraction of mitochondria were in close proximity to the exogenously dyed capillaries and that resting mitochondrial redox state was proportional to distance from capillaries. These results are consistent with an oxygen gradient, at rest, from the capillaries to the core of the muscle cell. The lower oxygen tension in the core may be an important adaptation to minimize free radical generation in resting muscle and to increase the sensitivity of metabolism to alterations in oxygen delivery.

Supplement Material

Sub-Cellular Motion Compensation for Minimally Invasive Microscopy, in vivo: Evidence for Oxygen Gradients in Resting Muscle – Online Supplement

Most *in vivo* microscopy preparations either observe tissue with thickness of less than 1 mm¹⁻⁶, or constrain tissue using a cover glass⁷⁻¹⁰. The motion compensation and analysis methods presented in this manuscript seek to expand the available tools for *in vivo* microscopy to observe novel tissue preparations and perform physiological experiments.

Supplemental Methods

Preparation of Optical Coupling Gel and Buffers

Carbomer gel was prepared with 300mM D-sorbitol (Sigma-Aldrich, St. Louis, MO) and 10mM HEPES free acid (Sigma-Aldrich, St. Louis, MO) in heated distilled water. A gelling agent, carbomer 940 (Snowdrift Farm, Tucson, AZ), was added to the heated sorbitol solution under constant stirring, to reach a concentration of 0.3%, based on a weight percent. Once the carbomer was completely dissolved in the solution, pH was adjusted by drop-wise addition of triethanolamine to 7.2-7.4. The gel was stored in a sealed container at 4°C.

Imaging buffer was prepared by adding 9 g/L of NaCl, 5 g/L of HEPES, and 5 g/L D-glucose (Sigma-Aldrich). Stock solutions of the calcium-release inhibitor and muscle relaxant and uncoupler were prepared to add to the buffer during the experiment. 5mg Dantrolene Sodium (Sigma-Aldrich, St. Louis, MO) was dissolved in 15 ml EtOH and

Supplement Material

when added to the imaging buffer brought concentration to 1 mM. 200mg of 2,4-dinitro-phenol, or DNP (Sigma-Aldrich), was dissolved in 45 mL EtOH, and when added to the buffer brought concentration in buffer to 1-2 mM.

Superfusion Setup

Superfusion buffer was placed in a heated chamber mounted ~50cm above specimen. Disposable tubing connected the buffer chamber to a water jacketed spiral tubing warmer (38deg. C) and from warmer to the objective. A small 2 mm internal diameter tubing was used for the final 10 cm to the objective and was taped to the side of the objective (Olympus 20x 0.95 NA). The objective was warmed with a 6 watt objective warmer and temperature controller (Bioptechs, Butler, PA). Buffer flow was adjusted to create laminar flow between objective point and tissue surface, as shown in Supplemental Figure I. A low molecular weight (M.W. 376) probe, disodium fluorescein (Sigma-Aldrich) at 50 μ M was used to validate diffusion from buffer to imaging plane (Supplemental Figure I).

Preparation of Animals

Anesthesia was induced by placing the mouse in a chamber (VetEquip, Pleasanton, CA) with 4% isoflurane. Once anesthetized, the mouse was placed on a surgery table heated using small disposable hand warmers wrapped in gauze, and anesthesia of 1.5-2% isoflurane was administered via nose cone. The tail vein was cannulated and 0.15 mL of 10 mM di-8-ANEPPS (Invitrogen), dissolved in 50/50 DMSO and EtOH, was gradually administered intravenously over 3 min (0.05 mL/min). The leg fur was removed using depilatory cream, and the skin above the tibialis anterior (TA) muscle

Supplement Material

was cut away (10-100 mm²). Two layers of fascia, the fascia sheath surrounding the anterior tibial bundle sheath and the TA epimysium, were delicately removed by gently abrading and peeling using small forceps. The exposed muscle was kept moist during surgery using saline buffer or a 0.3% carbomer gel. The opposite paw was monitored by a clip-on pulse oximeter probe (ITEC Engineering, Madison, WI). All experiments were performed in accordance with the National Institute of Health Guide for the Care and Use of Laboratory Animals.

Stage Setup

The mouse was placed in a modular setup on top of a 10kg capacity micro-positioning hexapod stage (M-840, Physik Instrumente, Karlsbad, Germany). The stage was heated in the same manner as the surgery table, and 1.5-2% isoflurane was again administered via nose cone. Several two-ball-jointed clamp arms (Kanetec, Bensenville, IL) were mounted at various points on the stage and be tightened down to hold the arm in arbitrary positions and angles. These arms had modified alligator clips (McMaster-Carr, Elmhurst, IL) that would hold the mouse's ankle, as well as secure the nose cone, cannula, etc.

Microscope Setup and Controller Operation

A Zeiss LSM 510 microscope (Carl Zeiss, Thornwood, NY) was adapted to interact with a separate real-time computer (RTC). The cable going from one non-descanned detector (NDD) was routed through a custom built high-bandwidth buffer board running a buffer-amplifier chipset (Maxim IC, Sunnyvale, CA). The video signal from the NDD along with trigger out information from the microscope user I/O cable was input to a

Supplement Material

video capture card (PCI-1410, National Instruments, Austin, TX) in the RTC, allowing the simultaneous acquisition of image data on the controller computer as well as the microscope computer. The 'Trigger 1' from the I/O cable was input to a multifunction I/O board (PCI 6251, National Instruments, Austin, TX) to maintain synchronization of the imaging cycle with the RTC.

A periscope (LSMTech, Eters, PA) with two rotary joints brought the light path from the upright microscope over to stage and down to the sample, with adjustable angles¹¹. The periscope was equipped with a piezo-motor (PIFOC-725, Physik Instrumente) to rapidly move the objective. The joints of the periscope were fitted with absolute rotary encoders (MAS-1024-N1, CUI, Tualatin, OR) to determine the orientation of the imaging planes relative to the stage.

In addition to the image information and the triggers coming from the microscope, the RTC had control of the objective focus motor via analog input and output of the multifunction I/O board. During the XY image acquisition, the motor would be stationary on the focal plane. During the XZ image acquisition, the motor would traverse a triangular path to 40 microns above and below the focal plane. The two images, XY and XZ would be compared on the RTC, and the offset would be translated into a distance to be moved. The RTC also had 12-bit digital inputs from the two encoders to determine angle of the images relative to the stage, and a serial communication (RS232) connection to the hexapod stage to send movement commands during tracking.

Imaging setup and Parameters

Supplement Material

The laser used for two-photon excitation was a pre-compensated¹² Ti:sapphire tuned to 720nm (Mai-Tai DS, SpectraPhysics, Newport, CA). The power was controlled by acousto-optical modulator to approximately 30-40% of maximum throughput, or 200-300 mW. Two channels were collected using non-descanned detectors with gain set to use full dynamic range of 12-bit pixels. The light path of both channels went through an IR blocking filter shortpass-680nm (Semrock, Rochester, NY). The tracking channel, channel 1, was put through a long-pass 515nm (Zeiss) while the data channel was put through a band-pass 430-490nm (Chroma, Rockingham, VT). The resulting 2 channels had good separation of ANEPPS and NAD(P)H.

The imaging parameters were set to allow interleaving of XY and XZ planes. On the LSM 510 this was 'time-series-bleach' mode. A bleach ROI of a single line (512x1 pixel) repeated 400 times after each XY image. The scanning galvomirrors would continue moving in X while the piezo motor moved in Z. The RTC would solely record the XZ image. The capillary vasculature was found to be an ideal pattern for tracking, since it has continuous spatial patterns, so that a small movement in the Y direction would not dramatically alter a subsequent XZ image. Also the vascular has adequate high spatial-frequency information to maintain tracking resolution, and could be labeled uniformly by exogenous dye.

Software and Algorithm

The real time computer ran LabVIEW (National Instruments) to control image acquisition, image analysis, and motor control. An offset was calculated between the maximum and the origin of the normalized cross-correlation between the current image

Supplement Material

and the reference image. This offset was translated into microns and adjusted to a proportion between 50% and 90% of the calculated motion, thus implementing a simple negative feedback loop control system. This tuning parameter was adjusted to ensure no oscillations occurred but also response was fast enough to track motion. The acquisition routine code, as implemented in LabVIEW, will be freely available by contacting the authors.

The performance of this prospective tracking method was dependent on the speed of acquisition, the speed of calculation, and the quality of the images. In this implementation, the maximum image frame rate was 0.6Hz for the two perpendicular planes when imaged at 512 x 512 and 512 x 200 pixels, respectively. Since computation time increased latency by one second, the amount of time between a given image and the response approached 2.5 seconds. Thus, to achieve frame-to-frame fidelity within 5 micrometers, this would limit maximum motion tracking to a speed to 2 micrometers per second. In observations of skeletal muscle, liver, kidney and brain, the drift movement following a physiological perturbation was generally is less than 100 micrometers per minute, so the speed of our tracking system provided adequate fidelity for most drift motion encountered. However, future implementations of this method that improved spatial resolution or incorporated respiratory and pulsa

tile gating would require faster image acquisition and analysis, which could be accomplished using resonant galvomirrors¹³ and parallel computational approaches¹⁴.

Supplement Material

The acquired images were processed using a deformable registration algorithm written in C++, with a wrapper implemented to use data in MATLAB (Mathworks). Channel 1 was used to calculate a vector motion map of how much each frame had deformed relative to a reference frame (See Supplemental Movie 5). The motion map was calculated by iteratively maximizing the local cross-correlation between representations of the images at different resolutions. This motion map was then applied to all frames of both the vasculature channel and the NAD(P)H channel, and the data was resampled to its original gridding using 2D interpolation with spline estimation.

Once data had been corrected for frame-to-frame motion, principal component analysis¹⁵ (PCA) was used to find trends in intensity changes in an unbiased method. First, data in each frame is mean adjusted. Each pixel's intensity through time is considered for the pattern of change relative to the mean and weighted into the principal components. There are as many resulting components as there are time points, and each of these components has a score for each pixel. The raw data can be completely reconstructed by multiplying each score image by its respective component value at that time point. However, most of these components are dominated by noise (Supplemental Figure II).

Supplemental Results

Motion Compensation

To demonstrate the system performance, we tracked a single field of view of a muscle *in vivo* during a saline infusion and recorded the amount of movement required to hold position. Then we repeated imaging without perturbation, but moving the field of view by the amount recorded previously. This resulted in an image sequence drifting across multiple cell layers, as the prior trial would have appeared without the motion compensation. A comparison of the prospectively tracked and non-tracked average vascular images reveals that the untracked image is an inaccurate presentation of the vascular structure due to the uncorrected motion (Supplemental Figure III). The overall signal to noise ratio of the tracked image was also improved since the same volume of the tissue was averaged. The same phenomenon is observed in the NAD(P)H channel. These data suggest that only the motion corrected data could be used to evaluate the vascular or mitochondria NAD(P)H topology in averaged data or in time course studies, *in vivo*.

As expected, random frame-to-frame motion was observed in the time-course images. The retrospective correction of in-plane deformations substantially increased the clarity of image averages by reducing the motion blur. The recovery of resolution in the motion corrected data is demonstrated by the visualization of muscle Z lines in the average image (Supplemental Figure III).

Supplement Material

Uncoupler Experiment

The tissue fluorescence associated with the maximum oxidized state of NAD(P)H was estimated using a metabolic uncoupler, dinitrophenol (DNP, 1-2 mM) that was superfused over the tissue directly below the objective using a flowing solution. Since local blood flow was maintained during time course imaging, the increase in reducing-equivalent flux could be maintained in the presence of uncoupler, and NAD(P)H was oxidized.

The DNP-treated NAD(P)H fluorescence levels in some subcellular regions decreased up to ten-fold as shown in Supplemental Figure IV. We found that the non-NADH(P)H background fluorescence was essentially zero following the superfusion of DNP. This is consistent with similar measurements in heart cells, where the non-NAD(P)H background after uncoupler was found to be negligible¹⁶. Thus, to determine the percent oxidation of NAD(P)H in this tissue, we assumed that there was no significant background fluorescence and zero fluorescence correlated with completely oxidized NAD(P)H.

Hypoxia Experiment

In our 6 datasets, In our 6 trials, there were 173 +/- 9 (SEM) time components (i.e. time points) which were mapped to an equal number of components, using PCA. The primary components explained 94.5% +/- 1.2% (SEM) of variability, the secondary components explained 2.0% +/- 0.4% (SEM) and all remaining components explained less than 1% of observed variability (see example in Supplemental Figure II). We eliminated all those components that account for less than 1% of total variance from the

Supplement Material

data. Since no other components reach significance, we can say that there is statistically complete description of available data using only the primary and secondary components. Thus, the primary and secondary components and their respective scores alone were used to reconstruct the filtered data. The first component represented the predominant change caused by the perturbation, and correlated well with mitochondrial structures (Supplemental Figure II), while the second component indicated that pixels in the field of view changed by differing percentages and was concentrated in the outer regions of the cells (Supplemental Figure II).

Since the secondary component is calculated based on residual data after best-fit of the primary component, to the extent that all of the voxels have the same kinetics, then these components will be linear combination of one another. This was apparently the case in these studies where the average linear correlation of the primary and secondary component was high, given the signal to noise, with an R^2 of $.73 \pm 0.07$. The fact that no other fluorescence time course other than the primary component was detected, we would argue that all of the mitochondrial pools had the same kinetic of change in hypoxia and that regional motion of the cells at the edges did not occur at a statistically significant level.

A back-projected movie of the data was created by multiplying both of the significant components by their score at each time point, and adding back the mean from that time point that had been previously subtracted. The back-projected data was used to calculate ratios of current NAD(P)H redox vs full oxidation at the post-perturbation plateau. An example of a back-projected dataset and the calculated his ratio for each frame is shown in Supplemental Movie 2. Our analysis of this ratio and the endpoint of

Supplement Material

the experiment was the basis for the calculation of the relative amount of change at each subcellular location.

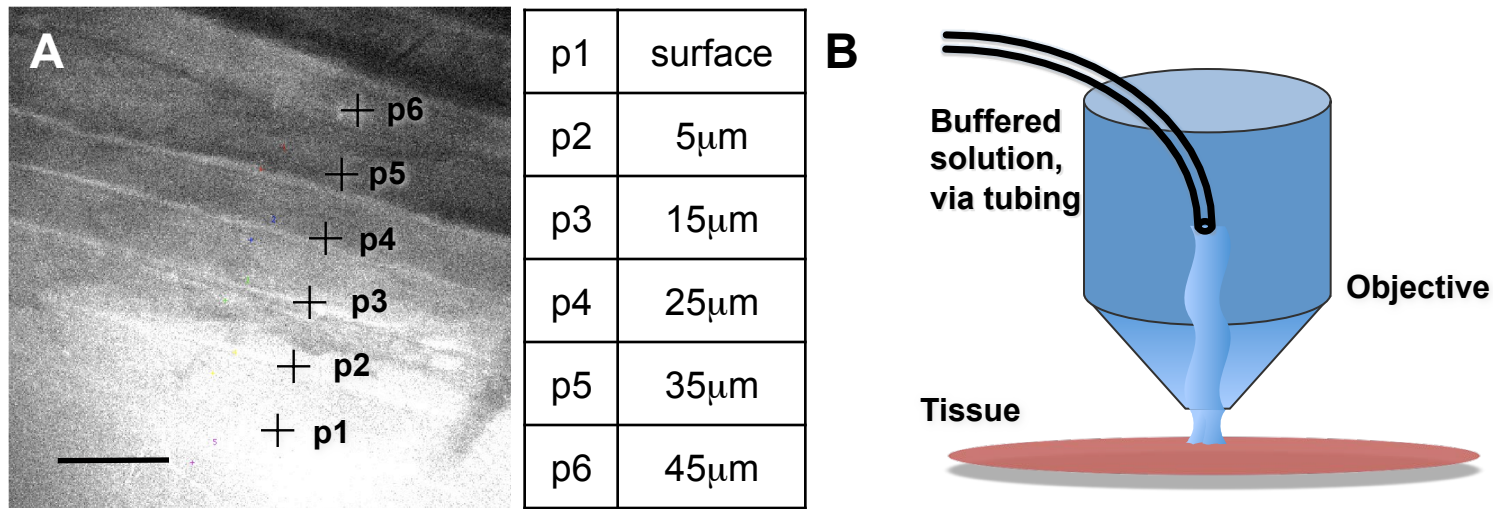
From our repeated viewing of all 6 experiments it was clear that the areas close to the vasculature had higher relative change in redox state. To illustrate this we surveyed the 6 datasets for all cells at which the imaging plane went through the center. The criteria for centered plane were the lack of crossing capillaries that would have indicated that the imaging plane cut near the surface, and a cell width not greatly exceeding the average, indicating extracellular space. The survey of datasets was based on the mean vasculature and mean back-projected NAD(P)H data, and 8 cells were selected (Supplemental Figure V). The resting redox state as a percentage of maximum oxidation was calculated at all pixels in each of the cells. The mean redox state down the length of each cell was calculated, with the left and right edges averaged as the 'cell edge mean' and a center line in the cell as the 'cell core mean.' Single cell oxygen-dependent NAD(P)H redox state fluorescence gradients similar to those observed in this study have also been observed in cardiac cells¹⁷ and the large muscle fibers of xenopus¹⁸, supporting the notion that the NAD(P)H redox gradient is generated by oxygen gradients in cells.

Supplemental References

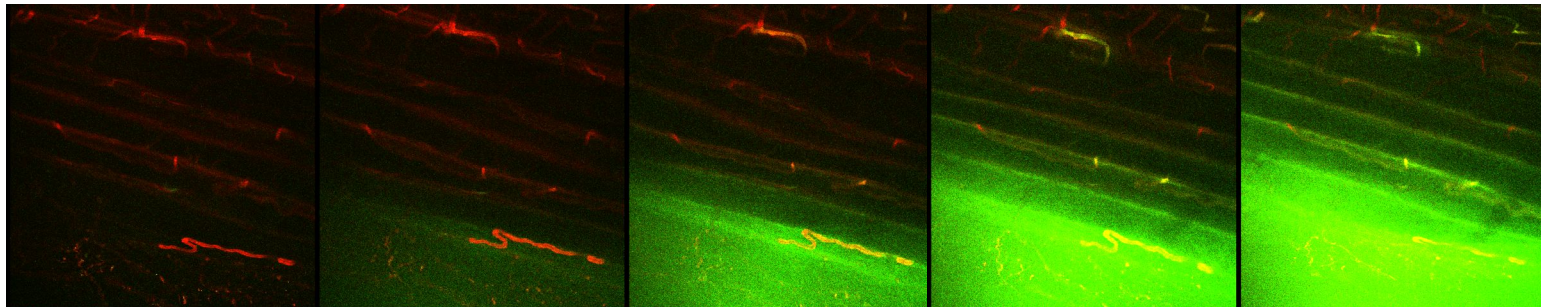
1. Hocking DC, Titus PA, Sumagin R, Sarelius IH. Extracellular matrix fibronectin mechanically couples skeletal muscle contraction with local vasodilation. *Circ Res.* 2008;102(3):372-379.
2. Rumbaut RE, Slaff DW, Burns AR. Microvascular thrombosis models in venules and arterioles in vivo. *Microcirculation.* 2005;12(3):259-274.

Supplement Material

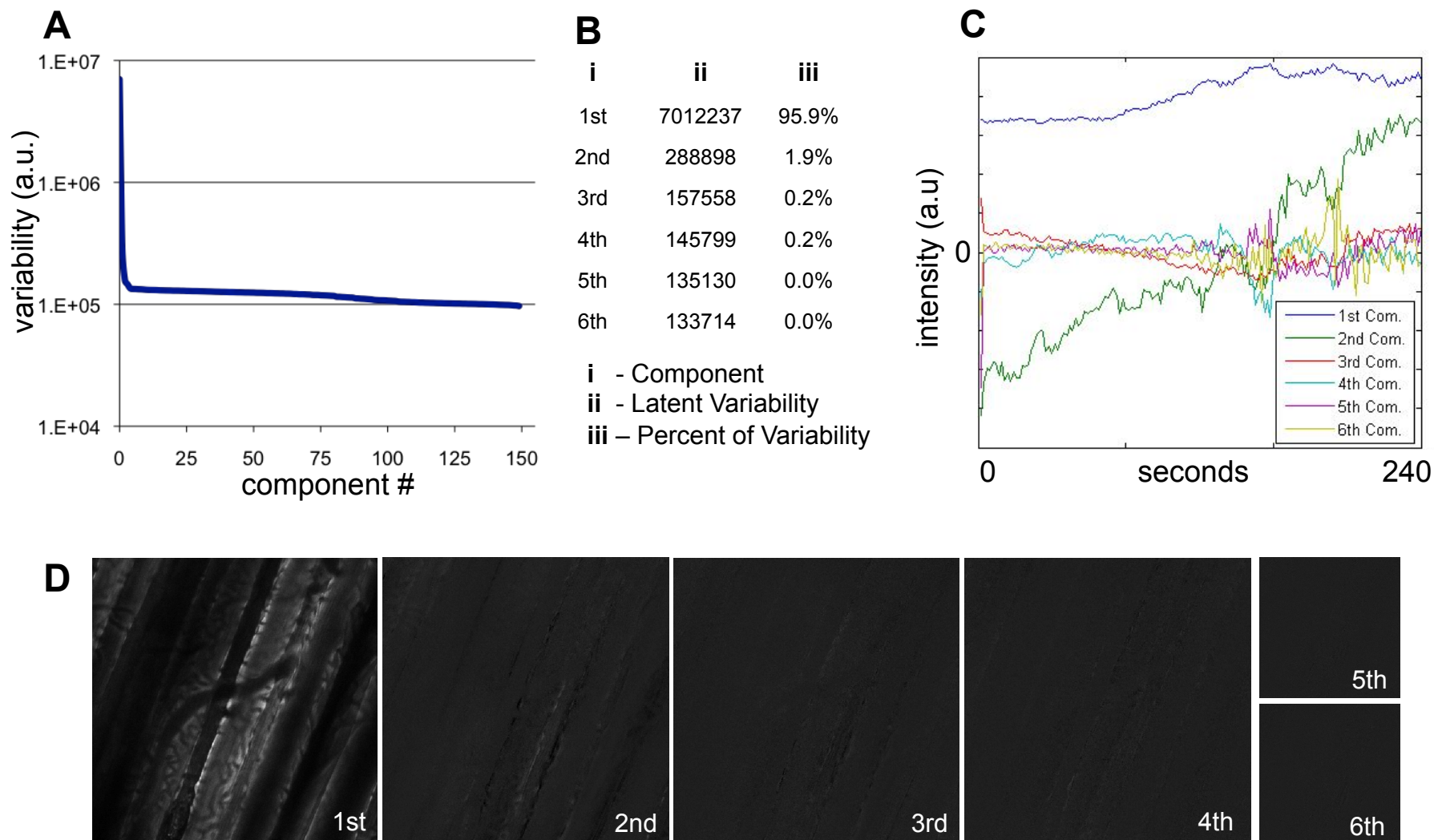
3. Figueroa XF, Chen CC, Campbell KP, Damon DN, Day KH, Ramos S, Duling BR. Are voltage-dependent ion channels involved in the endothelial cell control of vasomotor tone? *Am J Physiol Heart Circ Physiol*. 2007;293(3):H1371-1383.
4. Kuijpers MJE, Munnix ICA, Cosemans JMEM, Vlijmen BJV, Reutelingsperger CPM, Egbrink MGAO, Heemskerk JWM. Key Role of Platelet Procoagulant Activity in Tissue Factor-and Collagen-Dependent Thrombus Formation in Arterioles and Venules In Vivo Differential Sensitivity to Thrombin Inhibition. *Microcirculation*. 2008;15(4):269-282.
5. Hakim CH, Jackson WF, Segal SS. Connexin isoform expression in smooth muscle cells and endothelial cells of hamster cheek pouch arterioles and retractor feed arteries. *Microcirculation*. 2008;15(6):503-514.
6. Shepherd RK, Duling BR. Use of Ruthenium Red Staining to Detect Mast Cell Degranulation In Vivo. *Microcirculation*. 1995;2(4):363-370.
7. Tawadrous MN, Zimmermann A, Zhang XY, Wheatley AM. Persistence of impaired hepatic microcirculation after nonarterialized liver transplantation in the rat. *Microcirculation*. 2002;9(5):363-375.
8. Sun CK, Zhang XY, Sheard PW, Mabuchi A, Wheatley AM. Change in mitochondrial membrane potential is the key mechanism in early warm hepatic ischemia-reperfusion injury. *Microvasc Res*. 2005;70(1-2):102-110.
9. Zhang XY, Sun CK, Wheatley AM. A novel approach to the quantification of hepatic stellate cells in intravital fluorescence microscopy of the liver using a computerized image analysis system. *Microvasc Res*. 2000;60(3):232-240.
10. Lichtman JW, Magrassi L, Purves D. Visualization of neuromuscular junctions over periods of several months in living mice. *J Neurosci*. 1987;7(4):1215-1222.
11. Rothstein EC, Nauman M, Chesnick S, Balaban RS. Multi-photon excitation microscopy in intact animals. *J Microsc* 2006;222(Pt 1):58-64.
12. Fork RL, Martinez OE, Gordon JP. Negative dispersion using pairs of prisms. *Opt Lett*. 1984;9(5):150-152.
13. Leybaert L, de MA, Mabilde C, Sanderson MJ. A simple and practical method to acquire geometrically correct images with resonant scanning-based line scanning in a custom-built video-rate laser scanning microscope. *J Microsc* 2005;219(Pt 3):133-140.
14. Moreland K, Angel E. The FFT on a GPU. *Proceedings of the ACM SIGGRAPH conference*. 2003:112 - 119.
15. Jolliffe IT. *Principle Component Analysis*. NY: Springer; 2002.
16. Eng J, Lynch RM, Balaban RS. NADH fluorescence spectroscopy and imaging of isolated cardiac myocytes. *Biophys J* 1989;55:621-630.
17. Takahashi E, Endoh H, Ishikawa M, Kishi M, Doi K. Effect of myoglobin inactivation on intracellular gradients of NADH fluorescence at critical mitochondrial oxygen supply. *Adv Exp Med Biol* 2003;530:565-567.
18. Hogan MC, Stary CM, Balaban RS, Combs CA. NAD(P)H fluorescence imaging of mitochondrial metabolism in contracting *Xenopus* skeletal muscle fibers: effect of oxygen availability. *J Appl Physiol*. 2005;98(4):1420-1426.



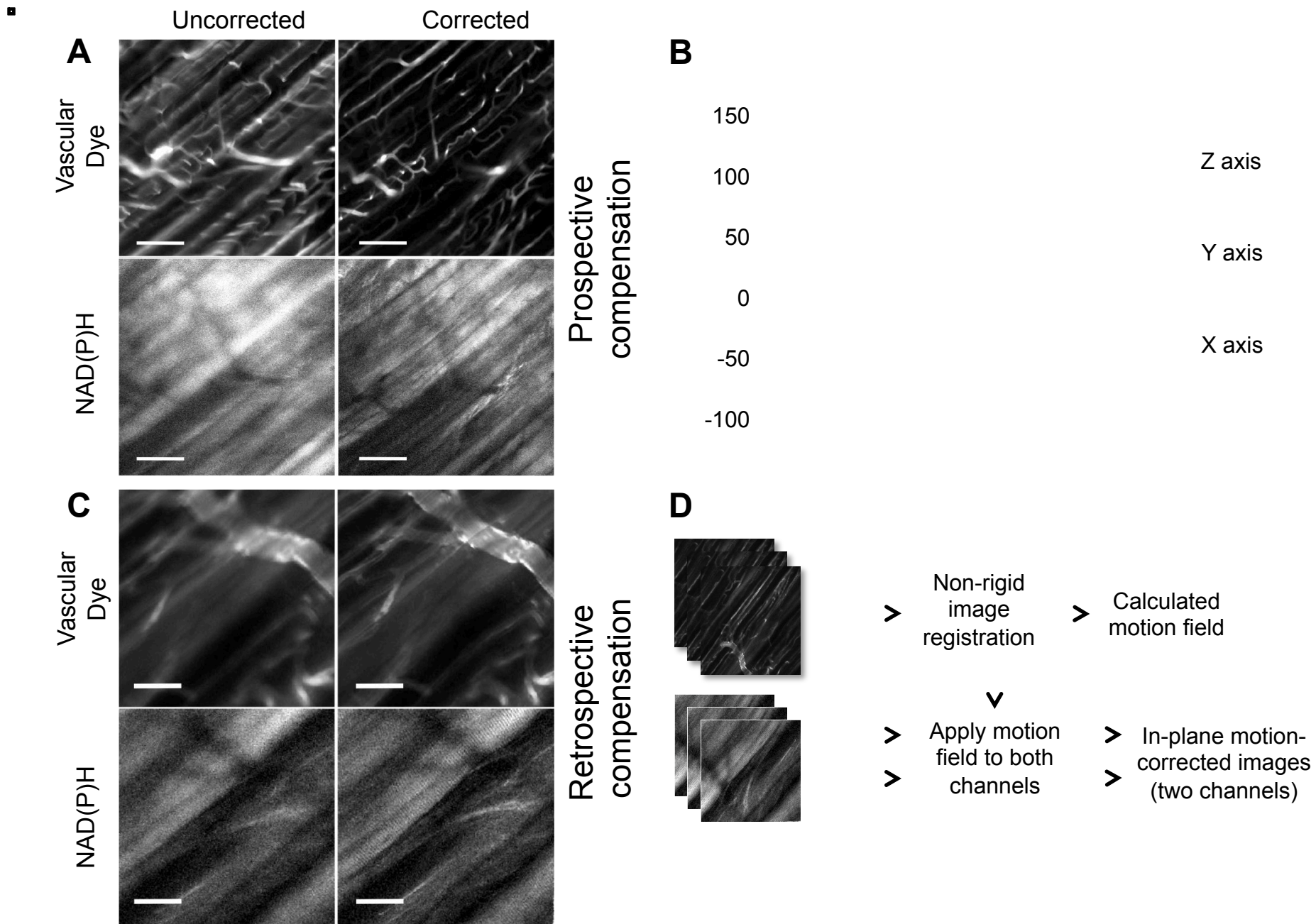
C



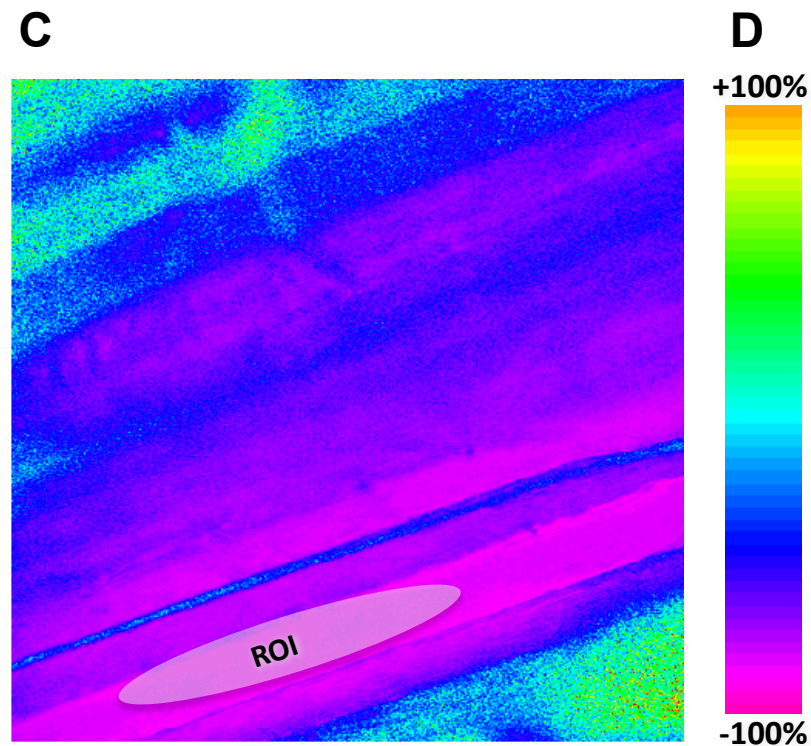
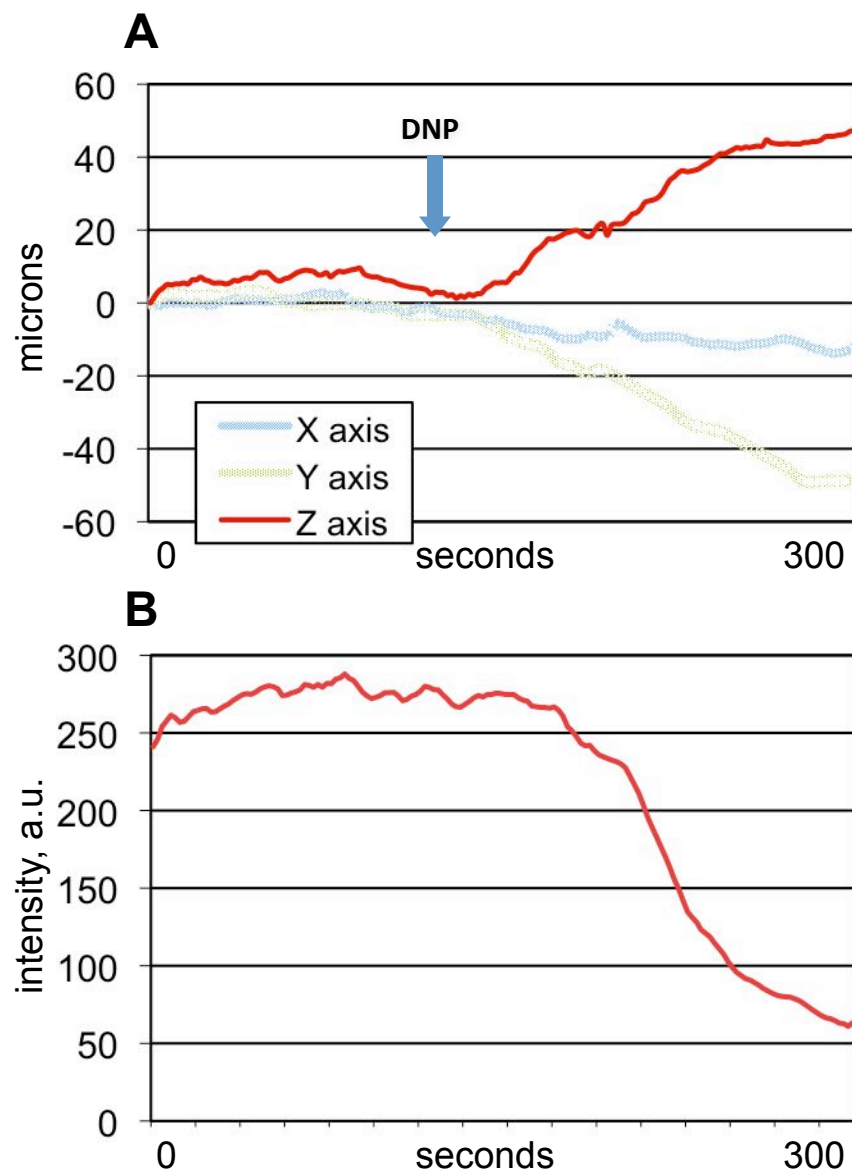
Supplemental Figure I: Delivery of small molecules via drip buffer **(A)** Image from time course of small molecule dye infusion. Imaging plane is skew relative to the muscle surface, so the bottom of field of view is at the surface while the top of the image is deeper within the muscle. Six points at varying depths below the surface as indicated. **(B)** Schematic of coupling interface, with water's simultaneous adhesion to the objective and tissue providing coupling medium for light as well as delivery of soluble compounds. **(C)** Images from two minute time-course during infusion of fluorescein, showing rapid increase of fluorescence and filtration at depths > 50 microns.



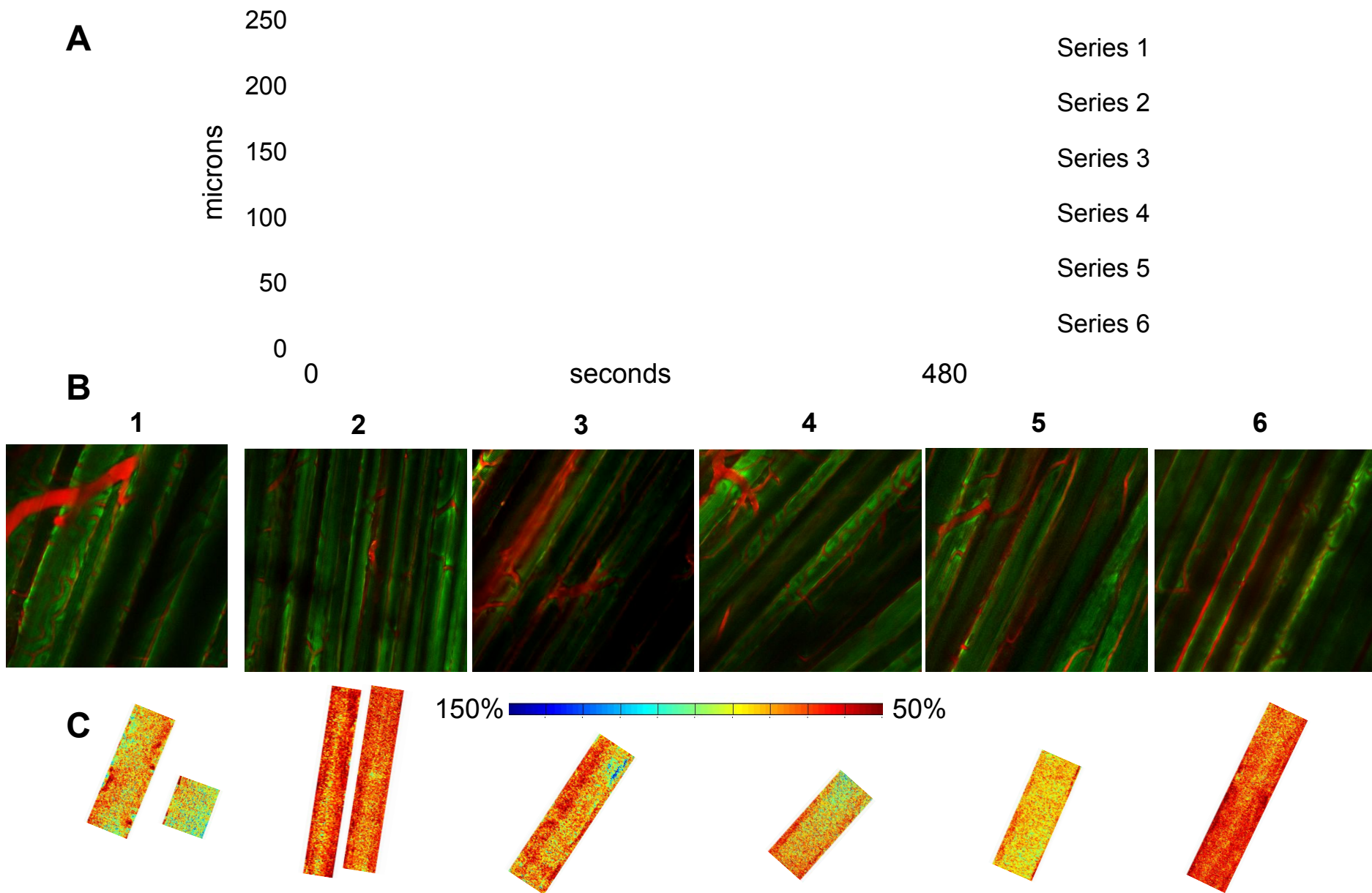
Supplemental Figure II: Principal component analysis **(A)** Latent variability graph, plotting latency (a.u.) vs. component number. Almost all variability can be described by only the first two components. **(B)** Table of first 6 components with latent variability and the percent of total variability described by that component. **(C)** Plotted first 6 components mean intensity (a.u.), vs. time of experiment (seconds). **(D)** Images of the scores of each of the first 6 components, showing decrease in signal to noise ratio in the scores of the less significant components. The significance threshold set for a given component to be included in reconstruction was accounting for greater than 1% of total variability.



Supplemental Figure III: Prospective and retrospective compensation results. Two-channel images **(A)** shown with and without correction using prospective motion compensation during motion **(B)**, following saline infusion. Scale bars 50 microns. Two-channel images **(C)** shown with and without correction using deformable registration retrospective compensation **(D)**. Scale bars 25 microns.



Supplemental Figure IV: Uncoupler experiments **(A)** Motion (in microns) of correction in X, Y, and Z during experiment. DNP added at time point indicated by arrow, total time 5 minutes **(B)** Mean of baseline corrected NAD(P)H signal (A.U.) during same time frame for ROI indicated **(C)** Map of calculated percentage change scores for each pixel, calculated via principal component analysis. **(D)** Lookup table of percentage change image from +100% (top) to -100% (bottom).



Supplemental Figure V: Net motion, filtered image data, and survey of percent change **(A)** Graph of total motion, $\Sigma \sqrt{(X^2+Y^2+Z^2)}$, in microns, vs. time for 6 experimental replicates. **(B)** Overlays of vasculature channel average (red) with filtered NAD(P)H data 6 experiments. **(C)** Cells from survey of all central cross section cells, with percent of intensity at rest, relative to fully oxidized state at hypoxia, calculated for each pixel.

Video Legends

Video 1: Two-channel time course, showing effect of registration

Video of two-channel acquisition during a representative hypoxia experiment. Left frames are vasculature with dye; right frames are NAD(P)H fluorescence. Images played at 24x speed, with entire sequence constituting four minute tracked acquisition. Amount of motion compensation for this experiment is shown in Figure 3. At $t=0$, nitrogen replaces oxygen in the ventilator and the onset of systemic hypoxia occurs during the first minute. Upper frames show both channels' raw acquisition from tracking microscope, while lower frames show in-plane motion corrected output after retrospective processing with the deformable image registration algorithm.

Video 2: Filtered NAD(P)H channel, expressed as ratio to starting conditions

Filtered data from NAD(P)H channel, from the same experiment segment as shown in Video 1. Upper frame shows back-projected image sequence after filtering out non-significant components of the principal component analysis (PCA), as described in Supplemental Methods. Lower frame shows PCA reconstructed data as a ratio of current frame vs. starting condition (first-minute-average), with a grayscale linear lookup table of -50% (black) to +400% (white).

Video 3: Rendering of ex-vivo muscle

Rendering of tibialis anterior from *in situ* scanning of muscle within the 15 minutes following death. Vasculature dyed with di-8-ANEPPS (red) and NAD(P)H autofluorescence (green). Rendered as maximum intensity projection using built-in Zeiss LSM 510 software.

Video 4: Image stack from ex-vivo muscle

Raw image data Z-stack, from same experimental images as used in rendering of Video 3, acquired as stack spanning 150 micrometers. Shows vasculature dyed with di-8-ANEPPS (red) and NAD(P)H autofluorescence (green).